Chemical Science

ROYAL SOCIETY OF CHEMISTRY

EDGE ARTICLE

View Article Online
View Journal | View Issue

Cite this: *Chem. Sci.*, 2025, **16**, 18233

All publication charges for this article have been paid for by the Royal Society of Chemistry

Tailoring multi-dimensional hierarchical self-assembly of metallacages through balancing non-covalent interactions

Xin Jiang, †[ab] Yaping Xu,†[a] Haixin Zhang, †[c] Hao Yu,[a] Ningxu Han, [a] Xu Guo,[a] Zinuo Gao,[a] Xinrui Zhang,[a] Haopeng Li,[d] Lei Ge,[e] Jiaqi Han,[b] Shaocheng Shen,[f] Jing Yu,*[d] Kun Wang,*[cf] Yunyan Qiu *[b] and Ming Wang *[a]

Despite advances in non-covalent interactions and complex self-assembly, precise control of multi-dimensional hierarchical self-assembly (HSA) from the molecular level to larger scales remains challenging. Herein, we designed and synthesized two rigid tetratopic ligands with multiple preset driving forces, and assembled them with Zn(II) ions to obtain metallacages **SC6** and **SC12**. Through balancing multiple non-covalent interactions, including metal–organic coordination, hydrophobic, and π–π interactions, **SC6** can hierarchically self-assemble driven by a poor solvent, from one-dimensional nanowires to super-helical nanostructures *via* non-equilibrium self-assembly, progressing continuously with time and the increasing proportion of the poor solvent. However, for **SC12** with enhanced hydrophobic interactions, two-dimensional monolayer nanogrids were formed by hierarchical self-assembly. Notably, these structures can be recycled back to primary metallacages through simple dissolution, highlighting their potential for efficient recycling and reuse. These results demonstrate that multi-dimensional hierarchical structures enable precise construction by balancing non-covalent interactions through a bottom-up self-assembly approach. This study provides deeper insight into the mechanisms of HSA and a promising strategy for the tailored creation of complex structures and sustainable porous materials.

Received 13th May 2025
Accepted 25th August 2025

DOI: 10.1039/d5sc03463a

rsc.li/chemical-science

Introduction

Nature demonstrates an extraordinary capacity to create highly organized and functional biological structures through hierarchical self-assembly (HSA). This intricate process leverages a limited array of building blocks and non-covalent interactions, enabling the construction of complex systems ranging from the nanoscale to the macroscale. This process is fundamental to living systems, exemplified by the supercoiling structures of DNA from paired deoxynucleotides,[1] construction of bacterial flagella from flagellin,[2] and the HSA process of amino acid sequences into triple helices to form collagen fibers[3] (Fig. 1a). Drawing inspiration from hierarchical structures in nature, researchers have developed a wide range of artificial hierarchical assemblies, including droplets,[4–8] vesicles,[9–12] fibers,[13–16] tubes,[17–22] and polymers.[23–30] Through the rational design of assembly units and non-covalent interactions, complex structures and functional carriers can be constructed, demonstrating significant structural diversity. However, the precise control of hierarchical structures remains challenging due to the complexity of thermodynamic and kinetic processes, as well as the combined influence of multiple non-covalent interactions.[31–35] Therefore, it has been challenging to replicate the stepwise assembly of living organisms from the nanoscale to more complex structures, especially the precise regulation of the HSA process step by step.

Discrete supramolecular structures are ideal building blocks for sophisticated assemblies because of their unique features, including (1) precise and well-defined shapes and sizes, allowing accurate control over the spatial arrangement and distribution of different components; (2) bottom-up synthetic strategies and remarkable reversibility, which avoid cumbersome synthesis and purification processes; (3) a wide range of non-covalent interactions—including metal coordination, electrostatic interactions, π–π stacking, hydrophobic interactions, hydrogen bonding, and van der Waals forces—that enable versatile and hierarchical self-assembly. Among

[a]*State Key Laboratory of Supramolecular Structure and Materials, College of Chemistry, Jilin University, Changchun 130012, China*
[b]*Department of Chemistry, National University of Singapore, 117543, Singapore*
[c]*Department of Physics, University of Miami, Coral Gables, Florida 33146, USA*
[d]*Mechano-X Institute, Applied Mechanics Laboratory, Department of Engineering Mechanics, Tsinghua University, Beijing 100084, China*
[e]*School of Materials Science and Engineering, Nanyang Technological University, 639798, Singapore*
[f]*Department of Chemistry, University of Miami, Coral Gables, Florida 33146, USA*
† X. J., Y. X., and H. Z. contributed equally to this work.

numerous types of interactions, coordination-driven self-assembly has been widely recognized and used since the early 1990s for constructing discrete metal–organic complexes (MOCs),[36–38] ranging from two-dimensional (2-D) polygons[39–44] to three-dimensional (3-D) cages.[45–54] The definite directionality and moderate bond energies of metal–ligand interactions enable well-defined and stable core geometries in MOCs.[37,55] These geometries can further facilitate orthogonal interactions with other non-covalent interactions, including hydrogen bonding, π–π stacking, hydrophobic interactions, and host–guest complexation, to achieve complex structures through HSA.[56,57] In recent years, several hierarchical structures based on coordination-driven assemblies as units have been reported, such as helical nanowires,[58] 2-D square arrays[59] formed by truncated cubic octahedra, and micrometer-scale ultrathin free-standing nanosheets formed by chiral metallacycles,[60] as well as hydrogels[61] and organogels[62–64] formed by metallacages. However, due to the complexity of multi-dimensional regulation, compatibility issues with multiple forces, and limitations in substructure stability, previous studies have primarily focused on analyzing the final product, and in-depth molecular-level insights often rely on theoretical simulations and calculations. Therefore, precise control of HSA processes and exploration of the deeper mechanism between initial units and hierarchical structures have remained elusive to date.

Inspired by the hydrophobic interactions and π–π stacking in the secondary structures of DNA to stabilize the helical structures,[65,66] we hypothesize that a similar collaborative interplay of multiple non-covalent forces can be programmed and tuned to control hierarchical self-assembly in artificial systems precisely. In this work, we designed and synthesized tetratopic ligands (**LC6** and **LC12**, Fig. 1c) that combine

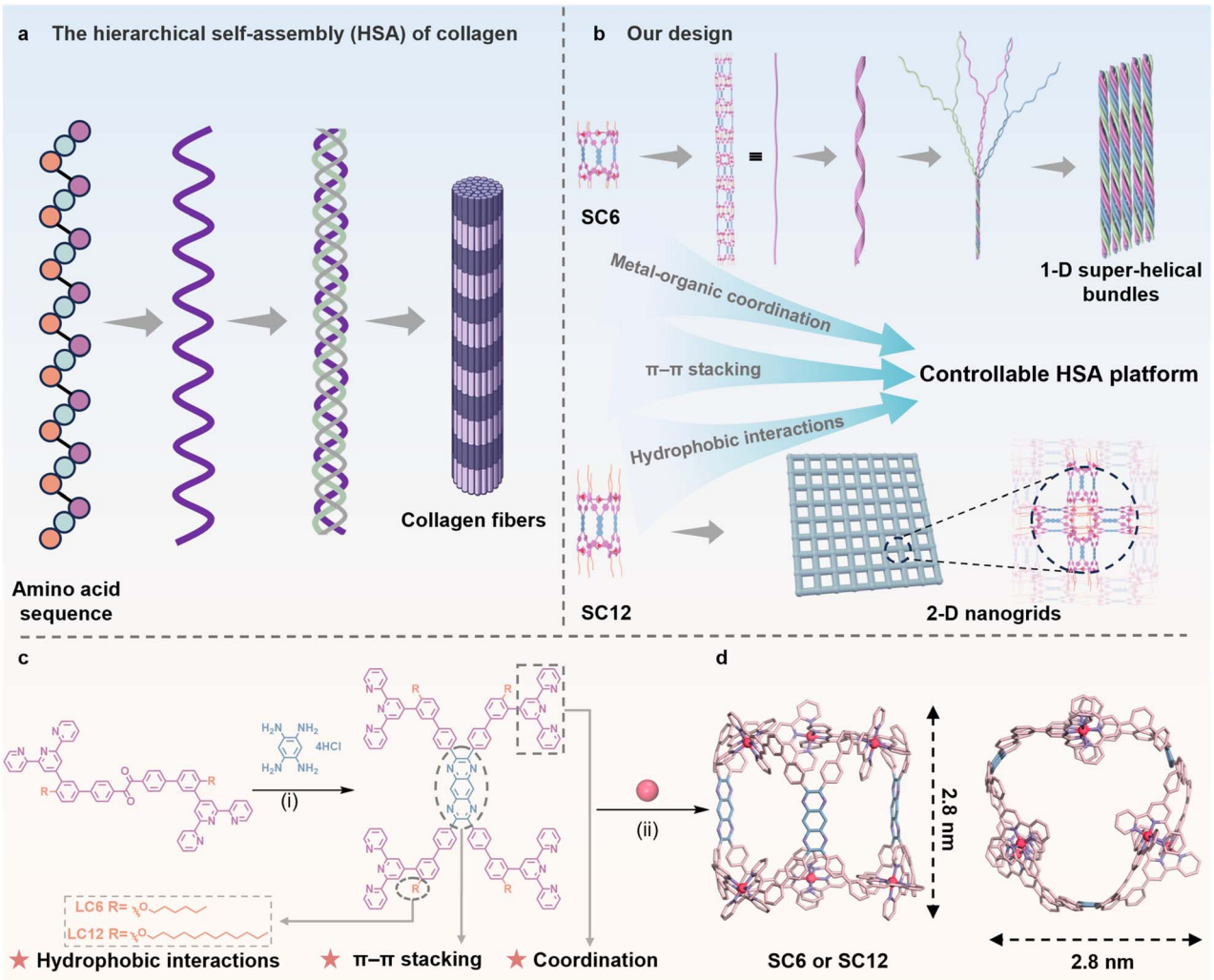

Fig. 1 (a) HSA spans from amino acid sequences to triple helices and collagen fibers in nature. (b) Our design of 1-D super-helical structures and 2-D nanogrids controlled by multiple interactions (metal–organic coordination, π–π stacking, and hydrophobic interactions) based on metallacages. (c) Synthesis of final ligands with multiple preset driving forces and their self-assembly with zinc ions. Reaction conditions: (i) precursors **4a** or **4b** (2.5 equiv.), 1,2,4,5-benzenetetramine tetrahydrochloride (1 equiv.), toluene/acetic acid (v/v = 1 : 1), 90 °C, 12 h, 72% yield for **LC6**, 64% yield for **LC12**; (ii) ligands **LC6** or **LC12** (1 equiv.), Zn $(NO_3)_2 \cdot 6H_2O$ (2 equiv.), chloroform/methanol (v/v = 1 : 3), 50 °C, 8 h, 92% yield for **SC6**, 90% yield for **SC12**; (d) schematic diagram of the energy optimal structure of the metallacages **SC6** and **SC12** (alkyl chains are omitted for clarity).

hydrophobic alkyl chains and rigid aromatic motifs within the same molecule. Upon coordination with Zn(II) ions, these ligands form discrete metallacages (**SC6** and **SC12**, Fig. 1d). The rigid aromatic core facilitates π–π stacking, while the terminal alkyl chains at both ends generate hydrophobic effects that promote longitudinal assembly. By synergistically tuning these interactions, **SC6** achieved stepwise self-assembly, gradually transforming from nanowires to super-helical structures (Fig. 1b). In contrast to the one-dimensional (1-D) hierarchical structures formed by **SC6**, the assembly of **SC12** further generated 2-D nanogrids, attributed to the increased hydrophobicity from the extended alkyl chains. Interestingly, not only can these hierarchical structures be regulated and captured, but they can also revert to their original metallacages upon redissolution in a good solvent. This multi-dimensional HSA regulation strategy offers deeper insight into emulating the complex structures and functions found in biological systems.

Results and discussion

Design, synthesis, and characterization of ligands and metallacages

Precursors **4a** and **4b** were synthesized by Suzuki–Miyaura coupling (Scheme S1) using compound 1,2-bis(4-(4,4,5,5-tetramethyl-1,3,2-dioxaborolan-2-yl)phenyl)ethane-1,2-dione with bromine-substituted terpyridine derivatives **3a** and **3b**. As shown in Fig. 1c, tetradentate ligands **LC6** and **LC12** were obtained by the efficient condensation of **4a** and **4b** with 1,2,4,5-tetraaminobenzene tetrahydrochloride respectively, incorporating the fused pyrazino[2,3-*g*]quinoxaline motif as a planar π–π stacking unit together with four free terpyridine units. Compared with **LC6**, **LC12** has a longer hydrophobic alkyl chain, which will influence the HSA structures due to enhanced hydrophobic interactions. After confirming the purity and structure of ligands, we next carried out the self-assembly with

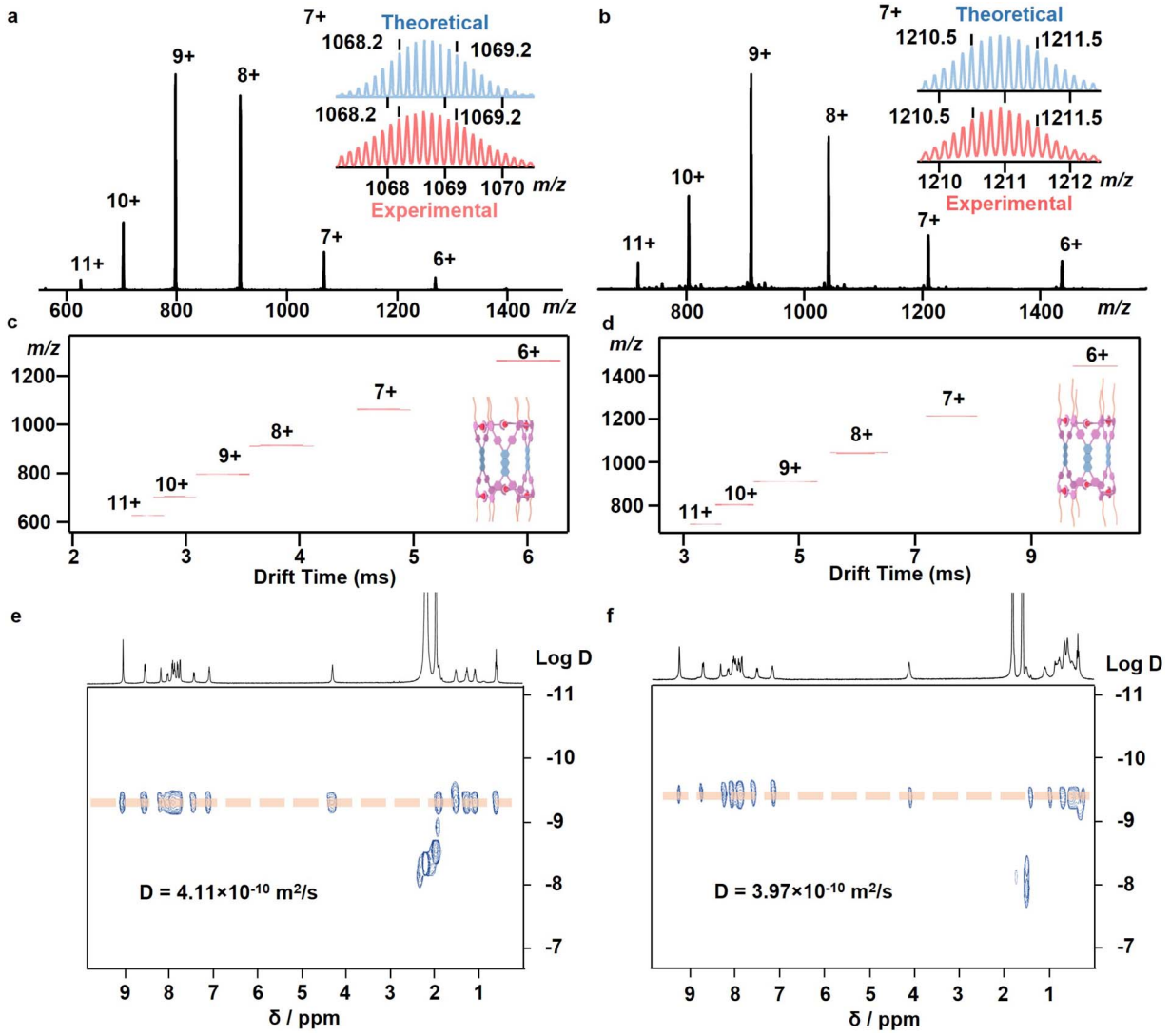

Fig. 2 Structural characterizations of metallacages **SC6** and **SC12**. (a) ESI-MS of complex **SC6** and (b) **SC12** (inset: theoretical and experimental isotope patterns for +7 ions). Two-dimensional TWIM-MS plots (*m/z vs.* drift time) of (c) **SC6** and (d) **SC12**. DOSY NMR spectra of (e) **SC6** and (f) **SC12** in CD_3CN at 298 K.

$Zn(NO_3)_2$ at a 1 : 2 molar ratio in a mixed solution of chloroform/methanol (v/v = 1 : 3) at 50 °C for 8 h. After counterion exchange with excess NH_4PF_6 (in MeOH), an orange-red precipitate was obtained. The precursors, ligands, and metallacages were fully characterized by ^1H, ^{13}C, and 2D-correlation spectroscopy (2D COSY) nuclear magnetic resonance (NMR) as well as high-resolution matrix-assisted laser desorption ionization time-of-flight mass spectrometry (HR-MALDI-TOF-MS) for ligands, electrospray ionization mass spectrometry (ESI-MS) for metallacages, density functional theory (DFT) calculations, and photophysical tests as shown in Fig. S1–S28.

Despite extensive efforts, the increased disorder induced by the alkyl chains has hindered the growth of high-quality single crystals. The chemical composition of the assemblies **SC6** and **SC12** was further confirmed by ESI-MS. As shown in Fig. 2a, for **SC6**, only one dominant set of peaks with different charge states (from +6 to +11) was observed, due to the loss of a different number of PF_6^-. The isotope pattern of each charge state closely matched the corresponding simulated isotope pattern of the metallacage (Fig. S27). The molecular weight of **SC6** was calculated to be 8468.1 Da, indicating the chemical composition of three **LC6**, six Zn(II), and twelve PF_6^- ($[Zn_{6LC6_3}]^{12+}\cdot[PF_6^-]_{12}$) was successfully formed. Traveling wave ion mobility mass spectrometry (TWIM-MS) showed only one set of signals, where each *m*/*z* value corresponds to only a narrow drift time distribution (Fig. 2c), suggesting that no other isomers or conformers were generated. The ESI-MS and TWIM-MS spectra (Fig. 2b, d and S28) demonstrated that **SC12** was also a trimer with a molecular weight of 9477.2 Da ($[Zn_{6LC12_3}]^{12+}\cdot[PF_6^-]_{12}$) without other isomers. In addition, the diffusion ordered spectra (DOSY) of

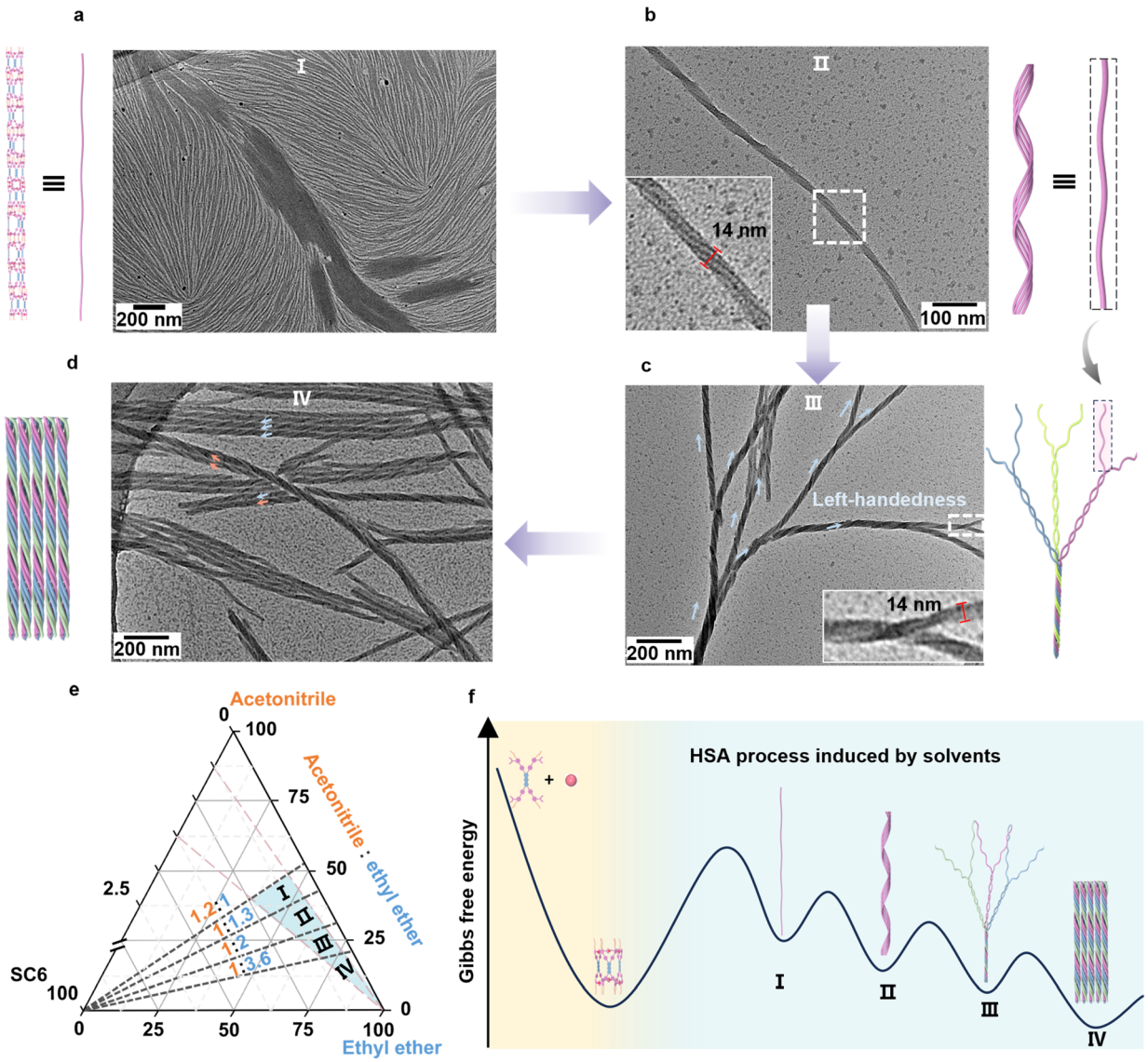

Fig. 3 Super-helices prepared by the HSA process induced by solvents. TEM images in the four stages of HSA, (a) stage of single-molecule nanowires, (b) stage of multiple nano-helical bundles, (c) stage of super-helical trees, and (d) stage of the final super-helical bundles (blue arrow: left-handedness; pink arrow: right-handedness). (e) Ternary phase diagram showing the HSA condition of solutions (light blue region) with acetonitrile, ethyl ether, and metallacage **SC6**. (f) Overview of the HSA process induced by solvents.

SC6 and **SC12** (Fig. 2e and f) all showed narrow bands with diffusion coefficient (D) values of 4.11×10^{-10} m^2 s^{-1} and 3.77×10^{-10} m^2 s^{-1}, respectively ($\log D$ values of -9.39 and -9.42), which also proves the formation of single discrete structures. The calculated diameters of **SC6** and **SC12** were 3.0 nm and 3.2 nm, respectively, which were larger than those of the ligands (Fig. S24 and Table S1). These values, estimated from the Stokes–Einstein equation based on an oblate spheroid model, are also consistent with the DFT calculation results in Fig. S25 and Table S2.

Control and characterization of 1D super-helices

Since metallacages combine the pyrazino[2,3-*g*]quinoxaline units and alkyl chains that enable strong π–π stacking interactions[67] and hydrophobic interactions, we focused on the mechanism and potential of their HSA. Herein, we used poor

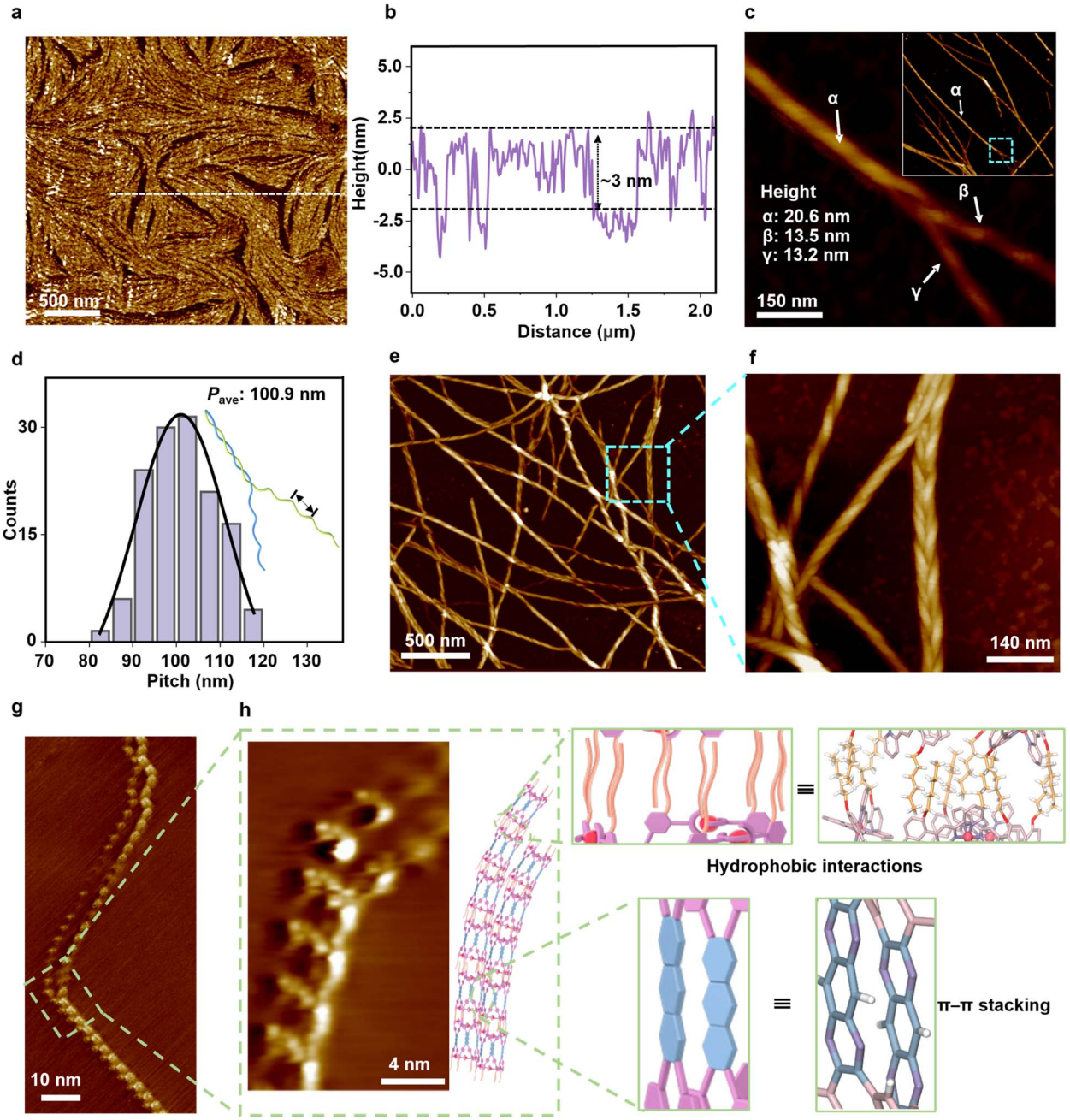

Fig. 4 AFM and STM images of HSA structures. AFM images for samples in (a) the stage of single-molecule nanowires. (b) The selection height map of nanowires. (c) Image of twisting into one super-helix α (Height: 20.6 nm). (d) Pitch distribution of helix β. (e) Stage of super-helical bundle formation. (f) Selected zoomed-in image of the super-helical bundles. (g) Image of the interaction between two single-molecule wires captured by STM. (h) The magnified view of the selected area of single-molecule wires interaction and speculative illustration of metallacages stacking mode.

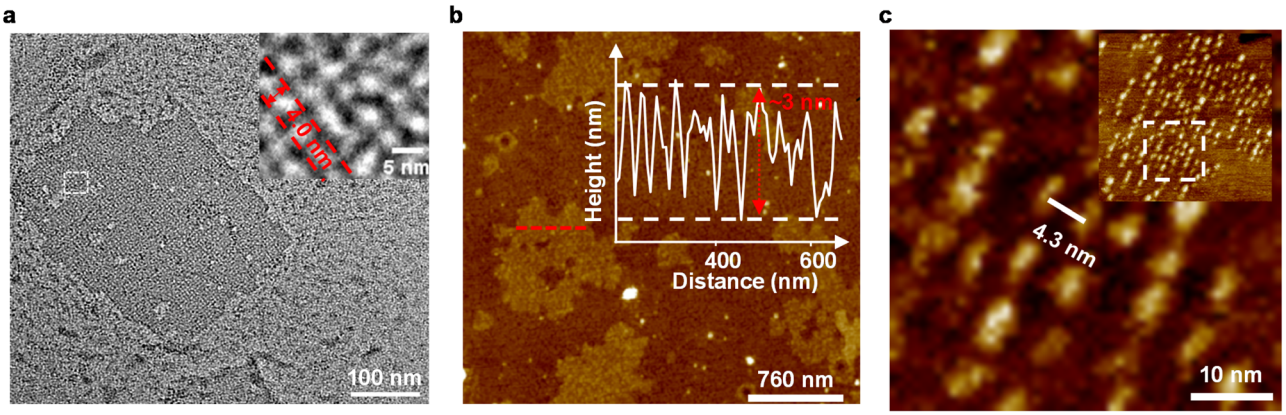

Fig. 5 Nanogrids formed by HSA. (a) TEM image of the final hierarchical morphology of **SC12**. (b) AFM phase diagram. (c) The selection height map of nanogrids.

solvent induction as the external driving force for HSA (Fig. S29). Slowly evaporating diethyl ether was introduced into the acetonitrile solution of **SC6** with a concentration of 1 mg ml^{-1} for several days, which was dropped onto a carbon-coated Cu grid for further characterization regularly by transmission electron microscopy (TEM). Conspicuously, **SC6** hierarchically self-assembled from single molecule nanowires into super-helical bundles, going through four sequential stages. In the first stage (after 2 days), we observed very thin nanowires (Fig. 3a), only a few nanometers in width and micrometers in length, which were arranged regularly, like fingerprints. Considering that the metal ions in the metallacages are accurately anchored on the surface, we speculate that the hydrophobic alkyl chains distributed in the upper and lower parts of

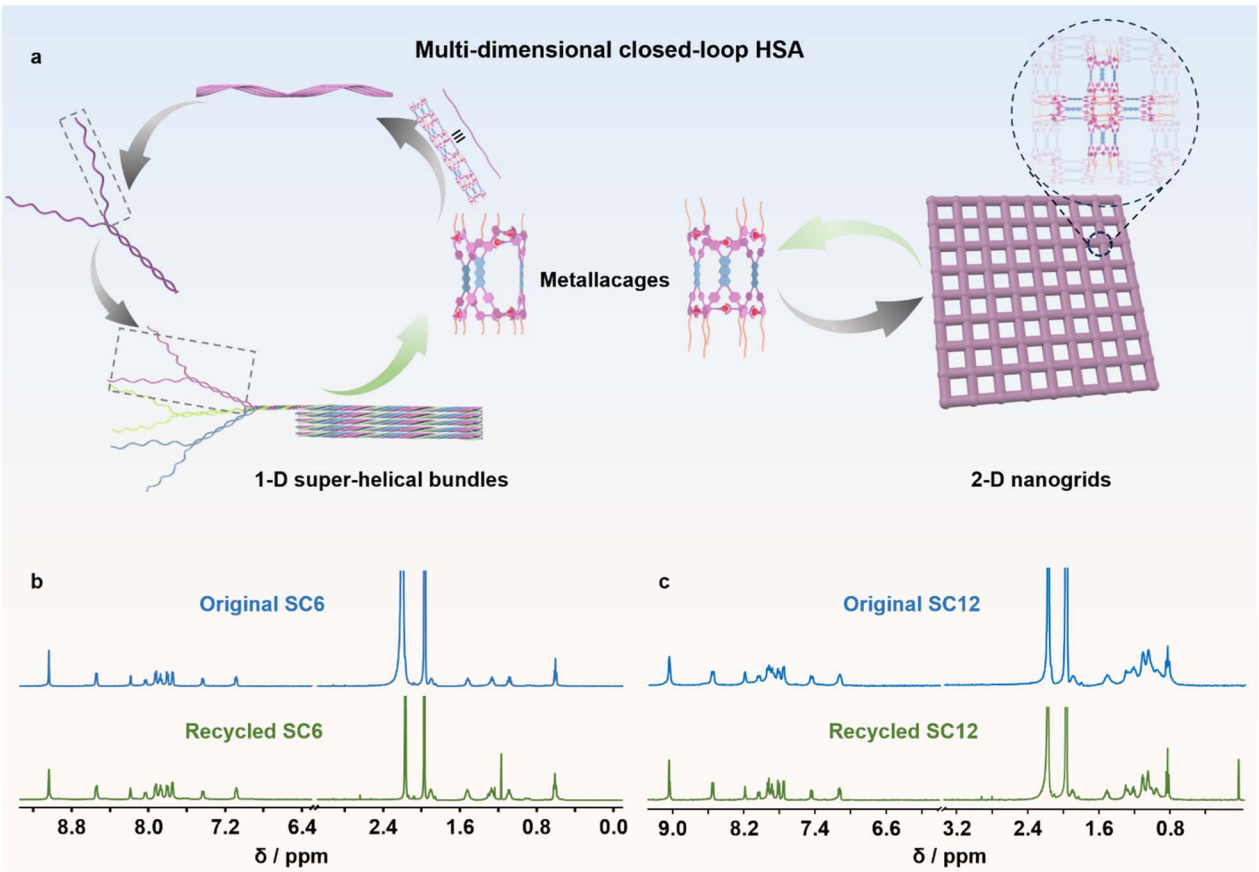

Fig. 6 (a) The schematic diagram of multi-dimensional closed-loop HSA. The ^{1}H NMR spectra of original and recycled metallacages **SC6** (b) and **SC12** (c) in CD_3CN at 298 K.

the metallacages promote their longitudinal arrangement, and the electrostatic repulsion generated by the counterions (PF_6^-) displaced around the metallacages maintains the regularly arranged morphology of the nanowires (Fig. S30).[68]

In the second stage (after 4 days), many helical bundles were observed. As shown in Fig. 3b and S31, four thin nanowires were wound into a helix, and the width, length, and pitch of the helices were about 14 nm, 1 μm or more, and 103 nm, respectively. With the further increase in the proportion of poor solvents, in the third stage (after 6 days), many clear super-helices were observed. As shown in Fig. 3c, two helices (*ca.* 14 nm in diameter) were intertwined into a double helix. As the degree of intertwining enhances, super-helical nanostructures were successfully obtained. Interestingly, "tree-like" helical nanostructures are formed after twisting of the helices. Based on numerous observations and statistical analysis, we found that helical structures growing on a super-helical tree had the same chirality. Fig. 3c and S32 showed the left-handed helical tree and the right-handed helical dendritic morphology, respectively. The diameter of the trunk was about 55 nm, and the length of the branches could reach 2 μm, which grew in a tightly intertwined manner with the same chirality based on geometrical complementarity with lower free energy.[69] Compared with the single-molecule nanowires in the first stage, we speculated that the π–π stacking of rigid pyrazine units between metallacages plays a key role in the formation of helical bundles and super-helical trees.

For the fourth stage (after 8 days), the continuous growth of super-helices stopped. The super-helices were largely arranged in parallel, and the morphology of the system remained unchanged after the fourth stage (Fig. 3d and S33). By analyzing TEM observations and detecting the ratio of solvents at different stages using NMR with varying initial concentrations of **SC6**, we identified the ratios of metallacage, acetonitrile, and ethyl ether for the formation of hierarchical self-assembly structures. We then illustrated a ternary phase diagram to depict the entire assembly process and the influence of solvents. There are the four stages I, II, III, and VI respectively which correspond to different multi-level structures (Fig. 3e). Notably, when the same proportion of poor solvent is added to the acetonitrile solution of **SC6**, the HSA structures of the corresponding stage cannot be obtained, suggesting that the whole process is a slow nucleation growth process, and it needs to continuously provide a poor solvent to the system, meaning a non-dissipative non-equilibrium multi-stage self-assembly process (Fig. 3f).[70–72]

To obtain more detailed structural information on the HSA of **SC6**, we further characterized it using atomic force microscopy (AFM). Through the same sample preparation procedure, we drop-cast the grown mixed solution onto the Si(111) substrate for AFM experiments. As shown in Fig. 4a, the thin nanowires observed in the first stage were consistent with those observed by TEM, with lengths in the micrometer scale. The height of the nanowire was measured to be ~3 nm as shown in Fig. 4b, which was consistent with the diameter of the metallacage (Fig. 1d). This further implied that the formation of the nanowires resulted from interactions between alkyl chains connecting the metallacages. Consistent with the TEM results, the AFM phase image also captured the HSA of intertwined nanowires to form helical trees and super-helical bundles. As shown in Fig. 4c and S34, the initial super-helix α was formed by twisting two helices β and γ, and its height was slightly smaller than the sum of the latter due to the geometric complementary forms of growth. A morphological statistical analysis calculated the pitch of helix β (P_{ave}) to be 100.9 nm as shown in Fig. 4d, which was consistent with TEM images. We also captured the end of the helices' growth to form dense super-helical bundles as shown in Fig. 4e, where the chirality was randomly distributed in this state (Fig. 4f), consistent with the phenomenon observed by TEM (Fig. 3d).

To gain molecular-level insights into the underlying self-assembly mechanism in the initial stage, we then employed a scanning tunneling microscope (STM) to image the self-assembly of **SC6**. The first stage assembled solution was deposited on the highly oriented pyrolytic graphite (HOPG) substrate by drop casting. As shown in Fig. 4g and S35, we successfully captured the formation process from single nanowires to double stranded nanowires. As illustrated in the magnified image (Fig. 4h), these two separated nanowires gradually approached and formed a double stranded nanowire. Notably, the two molecular wires are situated nearby, which might be attributed to possible π–π stacking interactions between pyrazino[2,3-*g*]quinoxaline motifs[72] between two metallacages, as illustrated in the cartoon. We speculated that this was also an important driving force for the subsequent formation of multi-stranded helices and super-helical structures. This also further proved that hydrophobic interaction was the main driving force for the formation of single-molecule nanowires as shown in the cartoon illustration. Therefore, with the assistance of STM imaging, self-assembling behavior is observed from the fundamental molecular scale. It makes up for the details of the further assembly of single nanowires that are not easy to capture in TEM and AFM.

Preparation and characterization of 2D nanogrids

In the thylakoid membranes of plants and cyanobacteria, light-harvesting complexes self-assemble into ordered 2D arrays of 5–10 nm, optimizing light capture and electron transport for photosynthesis.[73] Two-dimensional structures are critical in biological systems for the metabolism and preparation of advanced materials due to high specific surface area. To further explore the influencing factors of HSA and try to realize two-dimensional array self-assembly, we investigated the HSA of **SC12** modified with 12C alkyl chains by enhanced hydrophobic interactions. Following the same procedure as used for **SC6**, we slowly evaporated diethyl ether into the acetonitrile solution of **SC12**. As anticipated, 2D nanogrids instead of helices were observed by TEM. During the initial stage, the system did not acquire an ordered multi-level structure. In contrast to the assembly process of **SC6**, we speculated that the entropy increase caused by long alkyl chains was detrimental to the nucleation of π–π stacking;[74] it may require sufficient time and solvent-driven rearrangement to reach a stable state. In the final stage of growth (after 6 days), as shown in Fig. 5a and S36, the

internal structure appeared as a neatly arranged grid and the four corners of the grid had higher contrast than the edges, indicating Zn(II) ions were mainly concentrated in the four corners due to the strong contrast between metal ions and organic compounds. The diameter of the black spot measured in the partial enlargement was about 3 nm, and the distance between its parallel bands was about 4 nm. AFM characterization showed that the height of the 2D nanogrids was about 3 nm (Fig. 5b), consistent with the diameter of the metallacage, indicating that the obtained two-dimensional nanogrids were a single layer. STM imaging of **SC12** on the Au(111) surface also provided detailed molecular-level information for the nanogrid. The distance between adjacent metallacages can be measured by magnifying the selected area. This distance was approximately 4.3 nm (Fig. 5c), which agreed well with the TEM results. We proposed a kind of arrangement for these nanogrids based on the **SC12** molecular model and estimated the distance between parallel metallacages to be 4 nanometers (Fig. S37), which is consistent with the above measurements.

By comparing the HSA behaviors of **SC6** and **SC12**, we demonstrated that balancing multiple non-covalent interactions enables precise regulation of HSA and promotes the formation of complex multi-dimensional structures. Specifically, by harnessing the interaction between alkyl chains and electrostatic balance, **SC6** units initially align longitudinally, forming single-molecule nanowires. As these nanowires grow, the system gradually evolves towards a more stable configuration, where the nanowires twist into helices primarily driven by π–π stacking interactions. Due to the absence of a distinct chiral superiority, these nanowires can randomly twist into either left-handed or right-handed super-helices. Only homochiral helices can continue twisting, as their complementary geometric structures readily form low-energy stable structures. HSA transformations in different dimensions can be achieved by balancing non-covalent interactions. For **SC12**, enhanced interaction between the alkyl chains inhibits the nucleation of π–π stacking. As the growth progresses, the system undergoes constant self-correction to achieve a stable state. The dominant hydrophobic effect, along with the rigid and symmetrical skeleton of metallacages, finally leads to the formation of regular 2-D nanogrids.

Compared with porous frameworks including MOFs and COFs, the hierarchical structures driven by non-covalent interactions have a good dynamic characteristic, which means that the dissociation and reconstruction of the multi-level structure can be achieved without destroying the covalent bonds (Fig. 6a). In this system, after dissolution in acetonitrile again, the hierarchical structures can revert to the thermodynamically stable state, metallacages. As shown in Fig. 6b and c, the disassembly NMR spectra were consistent with the initial metallacages (Fig. S23), as well as the TEM images in Fig. S38 and S39, confirming that these hierarchical structures are not only tunable but also capable of assembly and recycling easily. This molecular-level understanding of HSA not only sheds light on the fundamental mechanism itself but also lays another approach for developing responsive smart materials or recyclable porous materials.

Conclusions

In this study, we synthesized rigid backbone ligands fusing pyrazino[2,3-*g*]quinoxaline and alkyl chains as multiple preset driving forces. These ligands, when coordinated with zinc ions, formed metallacages (**SC6** and **SC12**), which further self-assembled hierarchically into 1-D super-helical bundles and 2-D nanogrids. This hierarchical formation was driven by the synergistic balance of metal–organic coordination, hydrophobic interactions, and π–π stacking. The stable, rigid framework and the cooperative noncovalent interactions enabled the direct experimental visualization and modulation of the HSA process of metallacages through TEM, AFM, and STM, as well as the recovery of the primary metallacages. Although achieving precise control and construction of hierarchical structures remains a formidable challenge in the pursuit of assembling artificial cells and complex biological mimics from the molecular level, our strategy provides an instructive and viable approach for the stepwise construction of multi-dimensional hierarchical structures. Future work will continue to use this strategy to design and develop functional reversible porous materials. Overall, this work establishes a foundation for developing intricate, reversible supramolecular architectures and porous materials through balancing molecular–scale interactions.

Author contributions

In this work, M. W. and X. J. conceived and designed the experiments. X. J. conducted the synthesis of metallacages and structural characterization. Y. X. and X. J. conducted hierarchical self-assembly of metallacages. Y. X. performed TEM and AFM characterization of the hierarchical assembly. H. Z. and S. S. conducted the STM characterization. H. Y., H. N., X. G., Z. G., and X. Z. participated in part of the basic experiments. X. J., Y. X., H. Z., L. G., H. L., J. H., B. L., J. Y., K. W., Y. Q., and M. W. analyzed and interpreted the data. The paper was written through contributions of all authors. All authors have given approval of the final version of the paper for submission.

Conflicts of interest

There are no conflicts to declare.

Data availability

The data supporting this article have been included as part of the SI. Supplementary information: Synthetic details and characterizations of ligands and complexes including NMR, MALDI-TOF, ESI-MS, TEM, AFM, and STM. See DOI: **https://doi.org/10.1039/d5sc03463a**.

Acknowledgements

We gratefully acknowledge the support from the National Natural Science Foundation of China (22271116 and 22071079 for M. W.). Y. Q. acknowledges the support from the National

University of Singapore Presidential Young Professorship start-up grant (22-5759-A0001), National University of Singapore white space funding (22-5759-A0002), and the Ministry of Education, Singapore, under Academic Research Fund Tier 1 (23-0456-P0001) and Tier 2 (T2EP10124-0016). K. W. and H. Z. acknowledge financial support from the U.S. Department of Energy, Basic Energy Sciences (Award No. DE-SC0024924) and the University of Miami Start-Up Fund that enabled the STM studies. J. Y. acknowledge support from National Key Research and Development Program of China (2024YFA0919300). J. Y. thanks financial support from Xiaomi Foundation.

References

1 J. D. Watson and F. H. C. Crick, *Nature*, 1953, **171**, 737–738.
2 M. A. B. Kreutzberger, R. R. Sonani, J. Liu, S. Chatterjee, F. Wang, A. L. Sebastian, P. Biswas, C. Ewing, W. Zheng, F. Poly, G. Frankel, B. F. Luisi, C. R. Calladine, M. Krupovic, B. E. Scharf and E. H. Egelman, *Cell*, 2022, **185**, 3487–3500.e14.
3 V. Ottani, D. Martini, M. Franchi, A. Ruggeri and M. Raspanti, *Micron*, 2002, **33**, 587–596.
4 M. Abbas, W. P. Lipiński, J. Wang and E. Spruijt, *Chem. Soc. Rev.*, 2021, **50**, 3690–3705.
5 N. Gao and S. Mann, *Acc. Chem. Res.*, 2023, **56**, 297–307.
6 A. F. Mason, B. C. Buddingh', D. S. Williams and J. C. M. van Hest, *J. Am. Chem. Soc.*, 2017, **139**, 17309–17312.
7 H. Fu, J. Huang, J. J. B. van der Tol, L. Su, Y. Wang, S. Dey, P. Zijlstra, G. Fytas, G. Vantomme, P. Y. W. Dankers and E. W. Meijer, *Nature*, 2024, **626**, 1011–1018.
8 D. Wang, L. Zhou, X. Zhang, Z. Zhou, Z. Huang and N. Gao, *Angew. Chem., Int. Ed.*, 2025, e202422601.
9 C. G. Palivan, R. Goers, A. Najer, X. Zhang, A. Car and W. Meier, *Chem. Soc. Rev.*, 2016, **45**, 377–411.
10 Y. Zhu, B. Yang, S. Chen and J. Du, *Prog. Polym. Sci.*, 2017, **64**, 1–22.
11 H. Li, X. Qian, H. Mohanram, X. Han, H. Qi, G. Zou, F. Yuan, A. Miserez, T. Liu, Q. Yang, H. Gao and J. Yu, *Nat. Nanotechnol.*, 2024, **19**, 1141–1149.
12 H. Pan, C. Zhang, W. Jiang and Y. Zhou, *Angew. Chem., Int. Ed.*, 2024, **63**, e202404589.
13 J. D. Hartgerink, E. Beniash and S. I. Stupp, *Science*, 2001, **294**, 1684–1688.
14 L. Fan, J.-L. Li, Z. Cai and X. Wang, *Nat. Commun.*, 2021, **12**, 2375.
15 P. Roth, R. Meyer, I. Harley, K. Landfester, I. Lieberwirth, M. Wagner, D. Y. W. Ng and T. Weil, *Nat. Synth.*, 2023, **2**, 980–988.
16 X.-Y. Lou, K. Zhang, Y. Bai, S. Zhang, Y. Li and Y.-W. Yang, *Angew. Chem., Int. Ed.*, 2025, **64**, e202414611.
17 W. Hwang, J. Yoo, I.-C. Hwang, J. Lee, Y. H. Ko, H. W. Kim, Y. Kim, Y. Lee, M. Y. Hur, K. M. Park, J. Seo, K. Baek and K. Kim, *Angew. Chem., Int. Ed.*, 2020, **59**, 3460–3464.
18 M. Schappacher and A. Deffieux, *Science*, 2008, **319**, 1512–1515.
19 T. G. Barclay, K. Constantopoulos and J. Matisons, *Chem. Rev.*, 2014, **114**, 10217–10291.
20 Y. Zhao, H. Kawano, H. Yamagishi, S. Otake, Y. Itoh, H. Huang, E. W. Meijer and T. Aida, *J. Am. Chem. Soc.*, 2023, **145**, 13920–13928.
21 T. Saito, T. Kajitani and S. Yagai, *J. Am. Chem. Soc.*, 2023, **145**, 443–454.
22 S. Mahapatra, D. Qian, R. Zhang, S. Yang, P. Li, Y. Feng, L. Zhang, H. Wu, J. S. W. Seale, P. J. Das, P. K. Jha, K. L. Kohlstedt, M. Olvera de la Cruz and J. F. Stoddart, *J. Am. Chem. Soc.*, 2024, **146**, 21689–21699.
23 T. P. J. Knowles, T. W. Oppenheim, A. K. Buell, D. Y. Chirgadze and M. E. Welland, *Nat. Nanotechnol.*, 2010, **5**, 204–207.
24 D. J. Lunn, O. E. C. Gould, G. R. Whittell, D. P. Armstrong, K. P. Mineart, M. A. Winnik, R. J. Spontak, P. G. Pringle and I. Manners, *Nat. Commun.*, 2016, **7**, 12371.
25 Q. Zhang, Y.-X. Deng, H.-X. Luo, C.-Y. Shi, G. M. Geise, B. L. Feringa, H. Tian and D.-H. Qu, *J. Am. Chem. Soc.*, 2019, **141**, 12804–12814.
26 J. Liu, W. Duan, J. Song, X. Guo, Z. Wang, X. Shi, J. Liang, J. Wang, P. Cheng, Y. Chen, M. J. Zaworotko and Z. Zhang, *J. Am. Chem. Soc.*, 2019, **141**, 12064–12070.
27 Y. Gu, J. Zhao and J. A. Johnson, *Angew. Chem., Int. Ed.*, 2020, **59**, 5022–5049.
28 L. Shao, J. Ma, J. L. Prelesnik, Y. Zhou, M. Nguyen, M. Zhao, S. A. Jenekhe, S. V. Kalinin, A. L. Ferguson, J. Pfaendtner, C. J. Mundy, J. J. De Yoreo, F. Baneyx and C.-L. Chen, *Chem. Rev.*, 2022, **122**, 17397–17478.
29 A. J. Savyasachi, O. Kotova, E. T. Luis, A. D. Lynes, S. Mills, S. A. Bright, G. J. McManus, M. E. Möbius, D. C. Williams, R. Pal, J. J. Boland and T. Gunnlaugsson, *Chem*, 2025, **11**, 102321.
30 Y. Ren, S. Guan and X. Qu, *Angew. Chem., Int. Ed.*, 2024, **63**, e202317251.
31 K. Ariga, J. Li, J. Fei, Q. Ji and J. P. Hill, *Adv. Mater.*, 2016, **28**, 1251–1286.
32 K. Ariga, X. Jia, J. Song, J. P. Hill, D. T. Leong, Y. Jia and J. Li, *Angew. Chem., Int. Ed.*, 2020, **59**, 15424–15446.
33 G. Vantomme and E. W. Meijer, *Science*, 2019, **363**, 1396–1397.
34 J. Guo, S. T. Rich-New, C. Liu, Y. Huang, W. Tan, H. He, M. Yi, X. Zhang, E. H. Egelman, F. Wang and B. Xu, *Chem*, 2023, **9**, 2530–2546.
35 L. Ge, H. Xu, X. Jiang and J. Yu, *CCS Chem.*, 2023, **6**, 69–90.
36 M. Fujita, J. Yazaki and K. Ogura, *J. Am. Chem. Soc.*, 1990, **112**, 5645–5647.
37 T. R. Cook and P. J. Stang, *Chem. Rev.*, 2015, **115**, 7001–7045.
38 S. Chakraborty and G. R. Newkome, *Chem. Soc. Rev.*, 2018, **47**, 3991–4016.
39 J.-H. Fu, Y.-H. Lee, Y.-J. He and Y.-T. Chan, *Angew. Chem., Int. Ed.*, 2015, **54**, 6231–6235.
40 Z. Jiang, Y. Li, M. Wang, D. Liu, J. Yuan, M. Chen, J. Wang, G. R. Newkome, W. Sun, X. Li and P. Wang, *Angew. Chem., Int. Ed.*, 2017, **56**, 11450–11455.
41 H. Wang, Y. Li, N. Li, A. Filosa and X. Li, *Nat. Rev. Mater.*, 2021, **6**, 145–167.
42 Z. Zhang, Y. Li, B. Song, Y. Zhang, X. Jiang, M. Wang, R. Tumbleson, C. Liu, P. Wang, X.-Q. Hao, T. Rojas,

A. T. Ngo, J. L. Sessler, G. R. Newkome, S. W. Hla and X. Li, *Nat. Chem.*, 2020, **12**, 468–474.
43 Z. Jiang, B. Chen, H. Zhao, J. Wang, Q. Dong, F. Fu, D. Liu, Y. Li, G. R. Newkome, P. Wang and M. Chen, *J. Am. Chem. Soc.*, 2024, **146**, 16721–16728.
44 G.-Y. Wu, W.-T. Dou, F. Zheng and H.-B. Yang, *Coord. Chem. Rev.*, 2024, **519**, 216107.
45 M. M. J. Smulders, I. A. Riddell, C. Browne and J. R. Nitschke, *Chem. Soc. Rev.*, 2013, **42**, 1728–1754.
46 D. Fujita, Y. Ueda, S. Sato, N. Mizuno, T. Kumasaka and M. Fujita, *Nature*, 2016, **540**, 563–566.
47 Z. Wang, L. He, B. Liu, L.-P. Zhou, L.-X. Cai, S.-J. Hu, X.-Z. Li, Z. Li, T. Chen, X. Li and Q.-F. Sun, *J. Am. Chem. Soc.*, 2020, **142**, 16409–16419.
48 Y.-S. Chen, E. Solel, Y.-F. Huang, C.-L. Wang, T.-H. Tu, E. Keinan and Y.-T. Chan, *Nat. Commun.*, 2019, **10**, 3443.
49 S. Bhattacharyya, S. R. Ali, M. Venkateswarulu, P. Howlader, E. Zangrando, M. De and P. S. Mukherjee, *J. Am. Chem. Soc.*, 2020, **142**, 18981–18989.
50 M. Li, S. Jiang, Z. Zhang, X.-Q. Hao, X. Jiang, H. Yu, P. Wang, B. Xu, M. Wang and W. Tian, *CCS Chem.*, 2020, **2**, 337–348.
51 X. Jiang, H. Yu, J. Shi, Q. Bai, Y. Xu, Z. Zhang, X.-Q. Hao, B. Li, P. Wang, L. Wu and M. Wang, *CCS Chem.*, 2021, **4**, 2127–2139.
52 K. Wu, T. K. Ronson, P. Su, Z. Chen, L. Goh, A. W. Heard, X. Li, F. Klautzsch, C. A. Schalley, M. Vinković and J. R. Nitschke, *Nat. Synth.*, 2023, **2**, 789–797.
53 K. Wu, E. Benchimol, A. Baksi and G. H. Clever, *Nat. Chem.*, 2024, **16**, 584–591.
54 Q. Dong, F. Liu, J. Wang, E. Han, H. Zhao, B. Chen, K. Li, J. Yuan, Z. Jiang, M. Chen, Y. Li, D. Liu, Y. Lin and P. Wang, *Angew. Chem., Int. Ed.*, 2025, **64**, e202416327.
55 H. Wang, C. Guo and X. Li, *CCS Chem.*, 2021, **4**, 785–808.
56 S. Datta, M. L. Saha and P. J. Stang, *Acc. Chem. Res.*, 2018, **51**, 2047–2063.
57 N. Sasaki, J. Kikkawa, Y. Ishii, T. Uchihashi, H. Imamura, M. Takeuchi and K. Sugiyasu, *Nat. Chem.*, 2023, **15**, 922–929.
58 H. Wang, K. Wang, Y. Xu, W. Wang, S. Chen, M. Hart, L. Wojtas, L.-P. Zhou, L. Gan, X. Yan, Y. Li, J. Lee, X.-S. Ke, X.-Q. Wang, C.-W. Zhang, S. Zhou, T. Zhai, H.-B. Yang, M. Wang, J. He, Q.-F. Sun, B. Xu, Y. Jiao, P. J. Stang, J. L. Sessler and X. Li, *J. Am. Chem. Soc.*, 2021, **143**, 5826–5835.
59 L. He, H.-K. Hsu, L. Li, L.-T. Lin, T.-H. Tu, T.-G. Ong, G.-G. Liou and Y.-T. Chan, *Chem*, 2022, **8**, 494–507.
60 J. Dong, L. Liu, C. Tan, Q. Xu, J. Zhang, Z. Qiao, D. Chu, Y. Liu, Q. Zhang, J. Jiang, Y. Han, A. P. Davis and Y. Cui, *Nature*, 2022, **602**, 606–611.
61 I. Jahović, Y.-Q. Zou, S. Adorinni, J. R. Nitschke and S. Marchesan, *Matter*, 2021, **4**, 2123–2140.
62 N. J. Oldenhuis, K. P. Qin, S. Wang, H.-Z. Ye, E. A. Alt, A. P. Willard, T. Van Voorhis, S. L. Craig and J. A. Johnson, *Angew. Chem., Int. Ed.*, 2020, **59**, 2784–2792.
63 J. K. Wychowaniec, H. Saini, B. Scheibe, D. P. Dubal, A. Schneemann and K. Jayaramulu, *Chem. Soc. Rev.*, 2022, **51**, 9068–9126.
64 Z.-E. Zhang, Y.-F. Zhang, Y.-Z. Zhang, H.-L. Li, L.-Y. Sun, L.-J. Wang and Y.-F. Han, *J. Am. Chem. Soc.*, 2023, **145**, 7446–7453.
65 D. R. Davies, A. D. Gelinas, C. Zhang, J. C. Rohloff, J. D. Carter, D. O'Connell, S. M. Waugh, S. K. Wolk, W. S. Mayfield, A. B. Burgin, T. E. Edwards, L. J. Stewart, L. Gold, N. Janjic and T. C. Jarvis, *Proc. Natl. Acad. Sci. U. S. A.*, 2012, **109**, 19971–19976.
66 S. K. Albert, M. Golla, N. Krishnan, D. Perumal and R. Varghese, *Acc. Chem. Res.*, 2020, **53**, 2668–2679.
67 M. Chen, X. Hu, J. Liu, B. Li, N. L. C. Leung, L. Viglianti, T. S. Cheung, H. H. Y. Sung, R. T. K. Kwok, I. D. Williams, A. Qin, J. W. Y. Lam and B. Z. Tang, *Chem. Sci.*, 2018, **9**, 7829–7834.
68 Y. Tian, X. Yan, M. L. Saha, Z. Niu and P. J. Stang, *J. Am. Chem. Soc.*, 2016, **138**, 12033–12036.
69 Y. Sang and M. Liu, *Chem. Sci.*, 2022, **13**, 633–656.
70 S. A. P. van Rossum, M. Tena-Solsona, J. H. van Esch, R. Eelkema and J. Boekhoven, *Chem. Soc. Rev.*, 2017, **46**, 5519–5535.
71 Z. Li, M. Chen, Z. Chen, Y.-L. Zhu, C. Guo, H. Wang, Y. Qin, F. Fang, D. Wang, C. Su, C. He, X. Yu, Z.-Y. Lu and X. Li, *J. Am. Chem. Soc.*, 2022, **144**, 22651–22661.
72 A. Singh, P. Parvin, B. Saha and D. Das, *Nat. Rev. Chem.*, 2024, **8**, 723–740.
73 L.-S. Zhao, T. Huokko, S. Wilson, D. M. Simpson, Q. Wang, A. V. Ruban, C. W. Mullineaux, Y.-Z. Zhang and L.-N. Liu, *Nat. Plants*, 2020, **6**, 869–882.
74 P. Zhang, X. Xu, M. Zhang, J. Wang, G. Bai and H. Yan, *Langmuir*, 2015, **31**, 7919–7925.